

Probing Oxide-ion Mobility in the Mixed Ionic–Electronic Conductor $\text{La}_2\text{NiO}_{4+\delta}$ by Solid-State ^{17}O MAS NMR Spectroscopy

David M. Halat,[†] Riza Dervisoglu,^{†,‡} Gunwoo Kim,[†] Matthew T. Dunstan,[†] Frédéric Blanc,^{†,§} Derek S. Middlemiss,[‡] and Clare P. Grey^{*,†}

[†] Department of Chemistry, University of Cambridge, Lensfield Road, Cambridge CB2 1EW, United Kingdom

[§] Department of Chemistry, Stephenson Institute for Renewable Energy, University of Liverpool, Crown Street, Liverpool L69 7ZD, United Kingdom

[‡] Department of Chemistry, University of Warwick, Coventry, CV4 7AL, United Kingdom

[†] Current address: Institute for Molecules and Materials, Radboud University, Heyendaalseweg 135, 6525 AJ Nijmegen, The Netherlands

ABSTRACT: While solid-state NMR spectroscopic techniques have helped clarify the local structure and dynamics of ionic conductors, similar studies of mixed ionic–electronic conductors (MIECs) have been hampered by the paramagnetic behavior of these systems. Here we report high-resolution ^{17}O ($I = 5/2$) solid-state NMR spectra of the mixed-conducting solid oxide fuel cell (SOFC) cathode material $\text{La}_2\text{NiO}_{4+\delta}$, a paramagnetic transition-metal oxide. Three distinct oxygen environments (equatorial, axial, and interstitial) can be assigned on the basis of hyperfine (Fermi contact) shifts and quadrupolar nutation behavior, aided by results from periodic DFT calculations. Distinct structural distortions amongst the axial sites, arising from the non-stoichiometric incorporation of interstitial oxygen, can be resolved by advanced magic-angle turning and phase-adjusted spinning sideband (MATPASS) NMR experiments. Finally, variable-temperature spectra reveal the onset of rapid interstitial oxide motion and exchange with axial sites at $\sim 130^\circ\text{C}$, associated with the reported orthorhombic-tetragonal phase transition of $\text{La}_2\text{NiO}_{4+\delta}$. From the variable-temperature spectra, we develop a model of oxide-ion dynamics on the spectral timescale that accounts for motional differences of all distinct oxygen sites. Though we treat $\text{La}_2\text{NiO}_{4+\delta}$ as a model system for a combined paramagnetic ^{17}O NMR and DFT methodology, the approach presented herein should prove applicable to MIECs and other functionally important paramagnetic oxides.

1. Introduction

Mixed ionic and electronic conducting (MIEC) ceramics have shown promise in recent years as oxygen-transport membranes in solid oxide fuel cells (SOFCs) and for chemical looping applications.^{1–7} The use of mixed conductors—primarily perovskite-type oxides—as SOFC cathodes has been shown to improve oxygen reduction kinetics and thus enable device operation at lower temperatures.^{8,9} Typically, the advanced functionality of these mixed-conducting systems derives from the mutual influence of metal cation mixed valency and oxygen non-stoichiometry.¹⁰ While the latter property, manifesting as oxygen vacancies or interstitials, has been directly implicated in the bulk performance of MIECs, the mechanistic origins of oxide-ion conductivity often remain unclear at the atomic level. Atomistic simulations have provided insight into underlying interstitial- and vacancy-mediated contributions to ionic conductivity,¹¹ but direct experimental confirmation of these details of ionic motion remains a challenge.

Unlike conventional diffraction-based methods sensitive to long-range order, solid-state NMR spectroscopy can provide insight into local, atomic-scale distortions in solids, with direct relevance to ionic conduction.^{12–15} Moreover, exchange rates and activation energies for thermally-activated transport processes can be derived from NMR spectra acquired at variable temperature (VT-NMR). Our group^{16–21} and others^{22–30} have shown that solid-state ^{17}O VT-NMR in particular can enable detailed mechanistic studies of fast oxide-ion

conductors, subject to successful enrichment^{31,32} of samples with ^{17}O (natural abundance 0.037%). Moreover, as a spin-5/2 nucleus with moderate electric quadrupole moment, ^{17}O is sensitive to electric field gradients (EFGs) generated by local charge and bonding asymmetry, as quantified through site-specific quadrupole coupling constants (C_Q). This quadrupolar interaction can further discriminate amongst different coordination environments in diamagnetic oxides.³³

Similar ^{17}O NMR studies of *paramagnetic* oxides such as MIECs, however, have met with comparatively limited success.³⁴ In paramagnetic materials, electron–nuclear spin interactions lead to large Fermi contact (hyperfine) shifts and anisotropic dipolar broadening that complicate spectral detection, resolution and assignment. Previous reports have generally been confined to single crystal samples, with spectra often recorded at cryogenic temperatures.^{35–37} In a significant advance by Kong *et al.* (2015), the first ^{17}O magic-angle spinning (MAS) NMR spectra of paramagnetic transition metal complexes have been recorded and assigned.³⁸ In this work, we extend paramagnetic ^{17}O MAS NMR to perform advanced pulse sequence techniques and variable-temperature measurements on a model MIEC, $\text{La}_2\text{NiO}_{4+\delta}$, to explore the structural and mechanistic details of the oxide-ion transport in this material.

$\text{La}_2\text{NiO}_{4+\delta}$, a perovskite-derived K_2NiF_4 -type mixed ionic–electronic conductor, shows high oxygen transport across a large tem-

perature range and is an important candidate SOFC cathode material.³⁹ With both paramagnetic (axial O_{ax} , equatorial O_{eq}) and diamagnetic (interstitial O_i) oxygen sites, the system is an elegant model for initial ^{17}O MAS NMR studies of MIECs. (By a "paramagnetic" or "diamagnetic" site, we here refer to the presence or absence, respectively, of electron spin-bearing cations such as Ni^{2+} in the local (first shell) oxygen coordination environment.)

Structurally, $\text{La}_2\text{NiO}_{4+\delta}$ is a member of the Ruddlesden-Popper family and consists of alternating LaNiO_3 perovskite-like layers and " La_2O_2 " rocksalt-like layers in an offset $ABA'B'$ arrangement (Figure 1a). Equatorial oxygen sites lie within the perovskite plane; axial sites bridge the layers. Incorporation of interstitial oxygen within the rocksalt layers is remarkably facile, and affords a considerable range of oxygen hyperstoichiometry (δ)—reported from $\delta = 0$ to ~ 0.3 , with $\delta > 0.15$ for SOFC applications.^{40,41} Structural and magnetic properties are very sensitive to oxygen excess.^{42,43} In this work, therefore, we consider only the highly hyperstoichiometric phases most relevant for fast oxide-ion conduction in SOFC cathodes. We first show that incorporation of interstitial oxygen leads to distinct and well-resolved displacement of axial oxygen sites, and paramagnetic ^{17}O NMR is uniquely sensitive to these local structural distortions. Results from periodic density-functional theory (DFT) calculations are integral in the interpretation of the ^{17}O NMR spectra; the axial distortion leads to a splitting of calculated hyperfine shifts, as observed experimentally, and calculated C_Q values corroborate assignment of the O_{eq} and O_{ax} sites.

We next perform variable-temperature NMR to probe oxide-ion dynamics associated with the orthorhombic-to-tetragonal phase transition of $\text{La}_2\text{NiO}_{4+\delta}$ reported near 150°C . At the composition $\delta = 0.3$, Aguadero *et al.* have reported the phase transition temperature $T_p = 132^\circ\text{C}$.⁴⁴ We argue that this transition is directly correlated with the onset of rapid interstitial motion between 110°C and 130°C , a process for which we extract an activation energy $E_a = 0.59 \pm 0.07$ eV. In particular, fast exchange between interstitial and axial oxygen sites, as in the hypothesized interstitialcy mechanism of Chronopoulos *et al.*,⁴⁵ occurs simultaneously with the abrupt disappearance of the aforementioned local distortion. This in turn induces the disruption of the cooperative tilting of perovskite layers responsible for the long-range orthorhombic ($Fm\bar{3}m$) distortion, incoherently averaging the structure to the tetragonal ($I4/mmm$) phase. Our proposed model of oxide-ion dynamics at these temperatures involves two coupled motional processes—1) exchange between interstitial and axial sites, and 2) "rocking" of NiO_6 octahedra dynamically altering the displacement of axial and equatorial sites—that together determine the observed ^{17}O VT-NMR lineshapes. In summary, we report the first ^{17}O MAS solid-state VT-NMR spectra of a paramagnetic oxide-ion conductor—with DFT-aided assignment of the local structure and oxide-ion dynamics—which should ultimately enable future studies of functionally relevant paramagnetic oxides by similar methods.

2. Experimental and theoretical methods

2.1. Synthesis, ^{17}O -enrichment and characterization. Samples of $\text{La}_2\text{NiO}_{4+\delta}$ were prepared by a solid-state reaction route as described previously.^{46–48} Stoichiometric amounts of La_2O_3 (Alfa Aesar, REacton, 99.999%; pre-dried) and NiO (Aldrich, 99.999%) were mixed in a mortar and pestle, pressed isostatically, sintered in

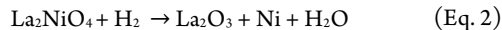
air at 1300°C for 6–12 h, and ground into powder. Multiple intermediate sintering and grinding steps were repeated until phase purity was achieved, as determined by laboratory powder X-ray diffraction (Figure S1).

Samples were also prepared *via* a modified sol-gel (Pechini) method similar to that previously reported.⁴⁹ Stoichiometric amounts of $\text{La}(\text{NO}_3)_3 \cdot 6\text{H}_2\text{O}$ (Alfa Aesar, REacton, 99.999%) and $\text{Ni}(\text{NO}_3)_2 \cdot 6\text{H}_2\text{O}$ (Aldrich, 99.999%) were dissolved in an aqueous solution of polyvinyl alcohol (15% w/v; Merck, MW = 60,000), with a mole ratio of metal cations to hydroxyl groups in polyvinyl alcohol of approximately 1:3. Continuous heating at 100°C produced a viscous green xerogel which was subsequently heated to autoignition at 400°C . The resulting off-black powder was pressed isostatically and sintered in air at 1300°C for 12 h. Sol-gel-synthesized samples did not differ appreciably in phase purity or excess oxygen content from samples obtained *via* the solid-state reaction route.

Samples of ^{17}O -enriched $\text{La}_2\text{NiO}_{4+\delta}$ were obtained by heating the as-synthesized powder (0.1–0.3 g) to 1000°C under an atmosphere of 70% $^{17}\text{O}_2$ (Cambridge Isotope Labs, used as received) in a sealed quartz tube for 24 h. Samples were slowly cooled ($1^\circ\text{C}/\text{min}$) from the enrichment temperature to maximize uptake of ^{17}O .

Phase purity of all samples was determined with powder X-ray diffraction (XRD) using a Panalytical Empyrean X-ray diffractometer equipped with a $\text{Cu K}\alpha$ source ($\lambda = 1.5406 \text{ \AA}$ and 1.5418 \AA) and X'celerator CCD detector. Scans were performed on a spinning sample stage in reflection mode over the range $2\theta = 5^\circ$ to 80° (step size $2\theta = 0.0167^\circ$). Diffraction patterns were analyzed with the X'Pert HighScore Plus software package and PDF pattern database, and Rietveld refinements were performed with the GSAS and EXPGUI software packages.^{50,51}

Oxygen excess (δ) in $\text{La}_2\text{NiO}_{4+\delta}$ was determined *via* thermogravimetric analysis (TGA) performed with a Mettler Toledo TGA/SDTA 851 thermobalance. Powder samples of 20–40 mg were placed in a $100 \mu\text{L}$ Al_2O_3 crucible and heated to 900°C (at 3°C min^{-1}) under a reducing atmosphere of 5% H_2 in N_2 (50 mL min^{-1}). Raw mass data collected during the heating profile were corrected from blank experiments and smoothed subject to a local regression (LOESS) algorithm. Sample non-stoichiometry was calculated as the ratio of mass losses during the two discrete reduction steps (Figure S2), where we assumed these mass losses correspond to the reactions



which were driven to completion given the gas flow conditions.⁵²

2.2. Solid-state NMR spectroscopy. Solid-state ^{17}O MAS NMR experiments were carried out on 7.05 T Bruker Avance II and Avance III 300 MHz spectrometers using a Bruker 4 mm HX probe (Fig. 1, 5); a 4.7 T Bruker Avance III 200 MHz using a Bruker 1.9 mm HX probe (Fig. 3); and a 16.4 T Bruker Avance III 700 MHz spectrometer using a Bruker 4 mm X probe (Fig. 4). Experimental parameters for all NMR data are summarized below.

Spin-echo mapping experiments at 7.05 T were performed under a MAS frequency of 12.5 kHz using a rotor-synchronized Hahn echo pulse sequence of the form $(\pi/6)_x - \tau - (\pi/3)_y - \tau$ —acquire with a pulse length of $1.67 \mu\text{s}$ ($\pi/6$ for liquid H_2O) at an inherent RF field strength of ~ 50 kHz and a quantitative recycle delay of 0.5 s. Similar experiments at 4.7 T were carried out at a MAS frequency of 40 kHz

using a pulse length of 0.75 μs ($\pi/6$ for liquid H_2O) at an inherent RF field strength of ~ 111 kHz, and a recycle delay of 20 ms. The pulse carrier frequency step size was 2500 ppm (~ 102 kHz at 7.05 T, ~ 68 kHz at 4.7 T), *i.e.* smaller than the RF field strength, and a total of six sub-spectra were acquired at 500, 3000, 5500, 8000, 10500, and 13000 ppm. Further spin-echo mapping experiments at 4.7 T employed longer pulse lengths of 2.2 μs ($\pi/2$ for liquid H_2O) at an inherent RF field strength of ~ 114 kHz, with identical pulse carrier frequency offsets. Finally, all other experiments not employing spin-echo mapping for broadband excitation (*i.e.* MATPASS or variable temperature measurements) fixed the pulse carrier frequency offset at 3000 ppm (at 7.05 T and 4.7 T) or 500 ppm (at 16.4 T). Standard saturation-recovery experiments (at 7.05 T) were used to obtain T_1 values.

Projection magic-angle turning and phase adjusted spinning sideband (MATPASS) NMR experiments⁵³ were performed at 4.7 T and were rotor-synchronized at a MAS rate of 40 kHz. A series of five $\pi/6$ (or $\pi/2$) pulses with pulse lengths of 0.73 μs (or 2.2 μs) were employed. A total of eight t_1 increments were recorded in each experiment. The recycle delay was 50 ms.

Temperature calibration of the probes was performed in separate one-pulse MAS experiments at 7.05 T and 16.4 T using the ²⁰⁷Pb resonance of $\text{Pb}(\text{NO}_3)_2$, with an accuracy of ± 5 $^\circ\text{C}$.^{54,55} All ¹⁷O NMR spectra were collected on recently ¹⁷O-enriched samples packed in ZrO_2 rotors with Kel-F or ZrO_2 caps (for room temperature and variable temperature experiments, respectively). ¹⁷O chemical shifts were externally referenced to H_2O at 0.0 ppm at room temperature. NMR spectra were processed and deconvoluted with the Bruker Topspin 3.2⁵⁶ and dmfit⁵⁷ software packages.

2.3. First-principles calculations. Calculations were performed with the CRYSTAL09 linear combinations of atomic orbitals (LCAO) code⁵⁸ using the B3LYP spin-polarized hybrid exchange-correlation functional. In a two-step approach, initial experimental structures were first geometry optimized with respect to lattice parameters and atomic positions using a more limited basis set (denoted BS-I). Next, single-point energy calculations were performed with an extended basis set (BS-II) to model the core region more accurately. Relevant NMR parameters (spin density at the nuclear positions, electron-nuclear dipolar tensors, and quadrupolar coupling constants) were computed after convergence of the wavefunction in the second step. Full details of the BS-I and BS-II basis sets are presented in the SI. For all calculations, truncation thresholds of 10^7 , 10^7 , 10^7 , 10^7 , and 10^{-14} were applied to the integral series for Coulomb overlap, Coulomb penetration, exchange overlap, g- and n-exchange penetration, respectively.

The experimental room-temperature orthorhombic ($Fmmm$) structure of $\text{La}_2\text{NiO}_{4+\delta}$ ($\delta = 0.17$)⁴¹ was used to construct a $2 \times 2 \times 2$ 57-atom supercell ($\text{La}_{16}\text{Ni}_8\text{O}_{33}$) corresponding to $\delta = 0.125$. The supercell was tetragonal due to expansion of the orthorhombic structure by $\sqrt{2}$ along new axes equivalent to $[110]_{Fmmm}$ and $[1\bar{1}0]_{Fmmm}$. Different initial $\text{Ni}^{3+}/\text{Ni}^{2+}$ configurations were explored with only minimal changes in the final optimized geometry, electronic structure, and computed properties. Ni^{3+} ions (d^7) were initialized in the low-spin configuration ($t_{2g}^6 e_g^1$, $S = 1/2$), as suggested by experimental evidence⁵⁹; calculations failed to converge in the high-spin configuration. Full structural optimizations of atomic positions and lattice parameters were performed without symmetry constraints, with convergence tolerances on the SCF cycle total energy, root-

mean-square (rms) gradient, and rms displacement of 10^{-7} au, 0.0003 au \AA^{-1} , and 0.0012 \AA , respectively. As a consequence of lattice anisotropy, reciprocal space sampling employed a compressed $3 \times 3 \times 2$ Monkhorst-Pack k-point mesh.

Two types of NMR parameters were extracted from the calculations: 1) quadrupolar coupling constants (and associated asymmetry parameters) and 2) hyperfine shifts for all oxygen sites. Quadrupolar coupling constants $C_Q = eQV_{ZZ}/h$ and asymmetry parameters $\eta_Q = \frac{V_{XX} - V_{YY}}{V_{ZZ}}$ were determined from the principal components of the calculated electric field gradient (EFG) tensor, ordered such that $|V_{ZZ}| \geq |V_{YY}| \geq |V_{XX}|$, where Q is the nuclear quadrupole moment (-25.58 mbarn for ¹⁷O, as experimentally determined⁶⁰). Values of the electron spin density at the oxygen nuclear positions were converted to hyperfine (Fermi contact) ¹⁷O NMR shifts using a theoretical methodology outlined previously.^{61,62} In brief, calculations were first performed in the ferromagnetic state by “locking” the alignment of the Ni spins, and then the system was allowed to relax in the absence of spin constraints to a ferromagnetic local minimum. Spin density values obtained from the relaxed system were then scaled to the paramagnetic regime at the temperature of the NMR experiment assuming ideal Curie-Weiss behavior. Experimental values of $\mu_{\text{eff}} = 2.56 \mu_B$ and $\Theta \approx -400$ K were used, as previously reported for $\text{La}_2\text{NiO}_{4+\delta}$.^{63,64}

3. Results

3.1. Characterization of $\text{La}_2\text{NiO}_{4+\delta}$ by XRD and TGA. Owing to the wide range of oxygen nonstoichiometry reported for this system, samples have been carefully characterized by XRD and TGA. Calculated values of δ from TGA measurements were found to range from $\delta = 0.12$ to 0.17 (Figure S2). The oxygen content is significantly affected by the ¹⁷O-enrichment procedure, increasing from $\delta = 0.12$ –0.14 for as-synthesized batches to $\delta = 0.15$ –0.17 following ¹⁷O-enrichment. Our work concurs with previous findings: treatment of $\text{La}_2\text{NiO}_{4+\delta}$ under high oxygen pressure leads to even more highly nonstoichiometric samples with δ as large as 0.3.⁶⁵

As-synthesized samples are found to be phase-pure by XRD (Figure S1). Laboratory XRD data are not sufficiently sensitive to the lighter O atoms to permit refinement of low-occupancy interstitial sites. Nonetheless, changes in the lattice parameters (as refined to the room-temperature $Fmmm$ structure) mirror differences in oxygen content, as previously shown.^{40,47,66,67} Here, incorporation of additional interstitial oxygen in the ¹⁷O-enriched samples leads to expansion of the lattice along c , with concomitant decrease of the a and b lattice parameters (Figure S3). The refined lattice parameters for the ¹⁷O-enriched samples are in good agreement with Skinner⁴¹ and also Aguadero *et al.*^{44,65} at similar levels of oxygen excess (that is, similar values of δ) determined by TGA.

Following ¹⁷O-enrichment, a weak, broad feature is observed in the XRD pattern, which is consistent with the (117) reflection of $\text{La}_4\text{Ni}_3\text{O}_{10}$ (Figure S1), suggesting that the $\text{La}_4\text{Ni}_3\text{O}_{10}$ impurity phase (estimated at ~ 3 wt. %) forms during the enrichment step. Aguadero *et al.* and Sayers *et al.* also note the decomposition of $\text{La}_2\text{NiO}_{4+\delta}$ into the higher-order Ruddlesden-Popper phases $\text{La}_3\text{Ni}_2\text{O}_7$ and $\text{La}_4\text{Ni}_3\text{O}_{10}$ at high temperature and under highly oxidizing conditions.^{65,68} Formation of these deleterious secondary phases may impair device longevity in functional SOFCs. In our case, these phases are difficult to distinguish from $\text{La}_2\text{NiO}_{4+\delta}$ (and from each other) due to the small phase fractions and considerable

overlap of XRD reflections (Figure S1c). We turn to NMR as a (potentially) more sensitive probe of the minor impurity phases as well as the local structure of the low-occupancy interstitial sites of $\text{La}_2\text{NiO}_{4+\delta}$.

3.2. Room temperature NMR. Acquisition of broadband spectra. Initial ^{17}O MAS NMR spectra of the enriched samples (Figure 1b) reveal an extremely broad set of features spanning more than 0.5 MHz at 7.05 T, exceeding the excitation bandwidth of a single RF pulse, a direct consequence of the paramagnetism of $\text{La}_2\text{NiO}_{4+\delta}$. Acquiring the complete broadband spectrum necessitates the use of "spin-echo mapping" or "variable offset cumulative spectroscopy", VOCS⁶⁹, here performed by collecting and summing six sub-spectra (colored traces, Figure 1b) with progressively larger RF carrier frequency offsets (step size equal to 2500 ppm or ~ 102 kHz). Pell *et al.* have shown that, for non-quadrupolar nuclei, spin-echo mapping under MAS achieves nearly uniform broadband excitation,⁷⁰ but no work to date has demonstrated the validity of the technique for quadrupolar nuclei such as ^{17}O . Given the significant width of the major features in our spectra, however, any lineshape distortions are likely insignificant, and the use of a short, non-selective rf pulse ensures quantitative excitation that is independent of C_Q . As seen in Figure 1b, the spin-echo mapped spectrum (black) comprises two very broad components centered at ~ 6500 ppm and ~ 3500 ppm, and a narrow peak at 532 ppm with associated spinning sideband (ssb) manifold. A minor component appears at 170 ppm (Figure 1c), but its intensity is sample-dependent (Figure S7).

Peak assignments. The resonances at 532 and 170 ppm fall within the 0–1000 ppm region occupied by shifts of diamagnetic oxides. Yang *et al.*⁷¹ have reported a ^{17}O shift of the tetrahedral oxygen site in hexagonal La_2O_3 of 584 ppm. Given the known⁷² pseudo-tetrahedral coordination of interstitial oxygen (O_i) in $\text{La}_2\text{NiO}_{4+\delta}$ (Figure 1a, bottom right), we, therefore, assign the 532 ppm feature to the interstitial oxygen environment in $\text{La}_2\text{NiO}_{4+\delta}$. We also assign the sample-dependent 170 ppm resonance to a very minor LaAlO_3 impurity phase (as previously reported by Bastow *et al.*⁷³) formed during synthesis (in an alumina crucible) but not immediately apparent in the XRD data. (Conversely, the $\text{La}_4\text{Ni}_3\text{O}_{10}$ impurity seen by XRD is not observed in our initial NMR experiments, but is later resolved in later high-temperature spectra as a minor feature at ~ 2400 ppm (see below).)

The highly shifted and broadened features at ~ 6500 ppm and ~ 3500 ppm are assigned to equatorial O_{eq} and axial O_{ax} sites, respectively (Figure 1a, top and middle right). These large hyperfine shifts are attributable to delocalization of unpaired electron spin density from the 3d orbitals of the $\text{Ni}^{2/3+}$ cations to the s orbitals of proximate ^{17}O nuclei: equatorial O_{eq} sites lying in the perovskite layer, with two nearby $\text{Ni}^{2/3+}$ cations at a short distance (~ 1.9 Å), are expected to experience a stronger hyperfine coupling than O_{ax} sites with only one directly bonded $\text{Ni}^{2/3+}$ further away (~ 2.2 Å). Additional support for this assignment comes from T_1 relaxation measurements, being sensitive to proximity to paramagnetic centers.⁷⁴ As expected, the T_1 value for the assigned O_{eq} site (< 500 μs) is noticeably shorter than that for O_{ax} (~ 1 ms). Finally, experimental evidence presented in Section 3.4 of a much larger quadrupolar coupling constant (C_Q) for O_{eq} is in good agreement with DFT-calculated values (Section 3.3), confirming the assignment.

We note that our assignment of the paramagnetic sites O_{eq} and O_{ax} in $\text{La}_2\text{NiO}_{4+\delta}$ agrees with previous static ^{17}O NMR results of the

isostructural cuprate $\text{La}_{1.85}\text{Sr}_{0.15}\text{CuO}_4$, with the higher frequency resonance assigned to equatorial oxygen in CuO_2 planes, and the lower frequency feature assigned to axial sites.^{75,76} However, the magnitude of the Fermi contact shifts is significantly smaller in the cuprate (equatorial: 1800 ppm; axial: 500 ppm), presumably as a consequence of reduced spin delocalization from Cu^{2+} , a cation with smaller magnetic moment than Ni^{2+} .

Quantification. All sub-spectra in Figure 1b have been recorded using a quantitative recycle delay (500 ms, at least 5 times T_1 for the O_i site) so as to compare intensity across different environments. To this end, we have fitted the broadband spectrum to a sum of two Lorentzian functions (justified simply because it provided the best fit) with associated satellite transition intensity for O_{eq} and O_{ax} and a CSA-only spinning sideband manifold for O_i (Figure S4). The integrated intensity ratio of the model, $\text{O}_{\text{eq}} : \text{O}_{\text{ax}} : \text{O}_i = 48 : 47 : 5 \approx 2 : 2 : 0.2$, agrees with the sample stoichiometry and is suggestive of a fully stochastic (*i.e.* not selective) ^{17}O -enrichment. A stochastic enrichment indirectly confirms fast ionic conduction involving all distinct oxygen sites in $\text{La}_2\text{NiO}_{4+\delta}$ at the enrichment temperature (1000 °C), as expected of a fast oxide-ion conductor. We also note that the relative integrated intensity of the O_i site (~ 0.2) concurs reasonably well with the oxygen excess calculated by TGA (0.15–0.17) given that we have not accounted for the signal lost from the paramagnetically-relaxed O_{eq} and O_{ax} sites during the refocusing period prior to acquisition, *i.e.*, we have not performed a spin-spin (T_2) relaxation correction. (We note that the short rf pulse length of $\pi/6$ is quantitative^{77,78} given the size of the C_Q values as determined later.) Finally, in comparing the weak LaAlO_3 signal to the O_i centerband intensity, we calculate the proportion of this minor impurity for this sample to be 0.7–0.8 mol%.

3.3. DFT calculations. First-principles periodic DFT calculations were performed to corroborate the argument for the given peak assignment, as well as to gain additional structural insights. Our $\text{La}_{16}\text{Ni}_8\text{O}_{33}$ supercell, corresponding to $\text{La}_2\text{NiO}_{4.125}$, contains a single interstitial oxygen defect (O_i) within one of the two rocksalt layers (Figure S5b). Following geometry optimization, we observe the rotation of the NiO_6 octahedra away from the neighboring interstitial defect. Frayret *et al.* have also reported interstitial-induced octahedral tilting in a compositionally identical supercell, corresponding to rotation along the $[100]_{I4/mmm}$ or, equivalently, $[010]_{I4/mmm}$ axes.⁷⁹ Our tilt axes could be described as being intermediate between the $[100]_{I4/mmm}$ and $[110]_{I4/mmm}$ directions, with the former dominant. Unlike the previous work, we observe minor tilting among octahedra not directly adjacent to the interstitial defect, possibly due to cooperative contraction of the unit cell along the stacking direction (*c*-axis).

Importantly, as also shown by Frayret *et al.*, O_{ax} sites directly adjacent to O_i are displaced away from the interstitial defect and slightly towards their respective Ni centers.⁷⁹ This differential displacement, correlated with proximity to the interstitial site, amounts to a splitting of the O_{ax} sites into different types. On the basis of Ni–O bond lengths, four O_{ax} types are identified, as depicted in Figure 2: (1) $\text{O}_{\text{ax},1}$, which are immediately adjacent to O_i ; (2) $\text{O}_{\text{ax},2}$, which are located within the same rocksalt layer as O_i but not adjacent to O_i ; (3) $\text{O}_{\text{ax},3}$, which are the oppositely positioned O_{ax} sites in the NiO_6 octahedra containing $\text{O}_{\text{ax},1}$; and (4) $\text{O}_{\text{ax},4}$, which are the oppositely positioned O_{ax} sites in NiO_6 octahedra containing $\text{O}_{\text{ax},2}$. The $\text{O}_{\text{ax},3}$ and $\text{O}_{\text{ax},4}$ sites are located within the "empty" (*i.e.* interstitial-free) rocksalt

layer and hence not directly displaced by the interstitial defect. Average Ni–O_{ax} bond lengths for the split sites (O_{ax,1} through O_{ax,4}) are 2.13, 2.16, 2.24, and 2.26 Å, respectively, as compared to the experimental value of 2.25–2.26 Å for the stoichiometric ($\delta = 0$) compound.^{72,80}

Although this axial distortion depends on subtle, long-range interstitial and charge ordering effects (SI, section 2), it strongly affects the calculated NMR parameters. Table 1 provides the average hyperfine shifts for equatorial, axial and interstitial sites. For each of the four O_{ax} types (labeled O_{ax,1} through O_{ax,4} in Table 1 and depicted in Figure 2) we calculate a distinct hyperfine shift, ranging from ~3200 to ~3900 ppm. Shifts are inversely correlated with the Ni–O_{ax} distance. Although distinct resonances cannot be resolved in our initial spin-echo mapped room temperature spectrum, where all O_{ax} sites appear within a single broad feature, the calculated hyperfine shift averaged amongst all axial sites (3539 ppm) is in good agreement with the experimental O_{ax} shift of ~3500 ppm.

The calculated shifts of the more distant equatorial oxygen sites are less influenced by the interstitial defect. In this case competing effects are at work: 1) a distribution of Ni–O_{eq} bond lengths due to lattice distortion of the -Ni–O_{eq}–Ni- chains, and 2) differences in spin density transfer to O_{eq} via the Ni $d_{x^2-y^2}$ orbital due to Ni^{2/3+} charge ordering. Moreover, the range of calculated hyperfine shifts across all O_{eq} sites is small relative to the average shift of ~10,000 ppm. In short, O_{eq} shifts do not cluster in distinct groups and, unlike the axial environments, cannot be easily classified by structural type. Nonetheless, the calculated hyperfine shift is much larger for O_{eq} than O_{ax}, as expected, confirming the spectral assignment. The theoretical and experimental shifts for O_{eq}, however, differ by nearly 4000 ppm. This large discrepancy is not entirely unreasonable; theoretical calculations of ¹⁷O hyperfine shifts in the solid state remain rudimentary, particularly at the level of hybrid DFT. Only Kong *et al.* have reported attempts for various paramagnetic coordination complexes, with results highly functional-dependent and with errors as large as 2500 ppm.³⁸ We believe the error is partly attributable to a non-optimal choice of functional (Kong *et al.* describe errors of nearly 6000 ppm before selection of an appropriate functional), but ultimately derives from the self-interaction error in DFT that enables excessive spin density delocalization onto the nearby O_{eq} sites.⁸¹ We also note that the higher concentration of Ni²⁺ in the theoretical supercell relative to experiment would increase the calculated O_{eq} (but not O_{ax}) shift. Additionally, residual antiferromagnetic couplings within the perovskite layers could lead to lower-than-predicted experimental O_{eq} shifts.

The interstitial site has a very small calculated hyperfine shift (of only 19 ppm), as expected, and hence the experimentally observed shift (of 532 ppm) is dominated by the chemical shift, not considered in these calculations.

Calculated quadrupolar coupling constants (Table 1) reflect the diversity of local charge and bonding asymmetry amongst oxygen environments. Typical values of C_Q for ¹⁷O nuclei in inorganic oxides vary from hundreds of kHz in highly symmetric alkaline earth oxides to 5–10 MHz in phosphates and chlorates⁸²; here, calculated C_Q's for La₁₆Ni₈O₃₃ span the known experimental range. The single interstitial oxygen site has a very nearly tetrahedral coordination to La³⁺, and a correspondingly small C_Q (0.38 MHz). By contrast, O_{ax} sites possess an octahedrally-coordinated geometry with five La³⁺ and one

Ni^{2/3+}. In this case the charge asymmetry (tri- vs. bivalent neighboring cations), distorted bond angles, and the short Ni–O_{ax} distance yield larger C_Q values. Furthermore, the axial displacement generating a distribution of Ni–O_{ax} bond lengths also yields distinct C_Q's for each split O_{ax} site, ranging from ~0.5 MHz to 2.4 MHz. Lastly, equatorial sites (O_{eq}) experience a locally octahedral environment as well, but with different neighbors: four La³⁺ and two Ni^{2/3+} in an axially compressed arrangement. Much shorter Ni–O_{eq} distances (1.9 Å) relative to La–O_{eq} (2.5–2.7 Å), combined with the effect of NiO₆ tilting distortions, give rise to a much larger C_Q (4.73 MHz).

3.4. Room-temperature MATPASS NMR with spectral editing. Suspecting from DFT calculations that additional spectral features could appear at higher resolution, we have performed further NMR experiments at faster magic-angle spinning (40 kHz). Spin-echo mapped spectra acquired at this spinning frequency now show evidence for overlapping spinning sidebands from additional sites (Figure 3, upper black trace). However, even with fast spinning, it is difficult to clarify details of the underlying fine structure due to spinning sideband overlap. The use of higher spinning speeds (*e.g.* 60 kHz) is unfortunately not feasible here, as the reduced sample volume would prohibitively increase acquisition time. Alternatively, experiments at lower magnetic field would increase the effective spectral distance between sidebands, improving resolution at a given spinning speed, but second-order quadrupolar effects would likely worsen resolution.

We therefore turn to a method of spinning sideband separation, (projection) magic angle turning and phase-assisted sideband separation, or MATPASS. This two-dimensional pulse sequence has been used by Hu *et al.* to obtain broadband "infinite"-MAS spectra in the case of large (>1 MHz) shift anisotropy.⁸³ The MATPASS experiment also succeeds in the familiar case of moderately quadrupolar nuclei (⁶Li, ⁷Li) in paramagnetic environments.⁵³ Applying the technique to ¹⁷O-enriched La₂NiO_{4+ δ} and extracting the isotropic slice (Figure 3, bottom black trace and Figure S6, inset) reveals six distinct paramagnetic features from ~3500–7000 ppm, in addition to the usual peak at 532 ppm previously assigned to O_i.

Since the calculated hyperfine shifts from DFT (Section 3.3) are not necessarily sufficiently accurate to discriminate amongst the different sites, we employ a form of spectral editing, quadrupolar filtering, exploiting the quadrupolar interaction to selectively suppress environments with large C_Q to aid in the assignments. This approach hinges on C_Q-dependent differences in quadrupolar nutation behavior, wherein sites with quadrupolar frequencies ν_Q much larger than the rf field strength ν_1 experience more efficient excitation by short rf pulses, on account of selective excitation of the central transition.⁸⁴ (For spin-5/2 nuclei, the quadrupolar frequency ν_Q is equal to $3C_Q/20$.) In practice, rf pulses with short flip angles will resolve all sites regardless of C_Q, whereas application of longer rf pulses (*e.g.* $\pi/2$ for a liquid reference) will preferentially select small-C_Q environments. Kentgens has shown that for spin-5/2 nuclei, a value of $\nu_Q \geq 6\nu_1$ is a reasonable threshold for full attenuation of signal using a longer, $\pi/2$ pulse (calibrated on a liquid reference).⁷⁷ In our case, where $\nu_1 = 114$ kHz, this corresponds to a threshold C_Q of 4.6 MHz.

Repeating the MATPASS experiment using a longer $\pi/2$ pulse (bottom blue trace, Figure 3), we observe the loss of the paramagnetic feature centered at 6860 ppm; we conclude that the C_Q of this site must equal or exceed 4.6 MHz. Amongst all DFT-calculated C_Q's, only that of O_{eq} (4.73 MHz) does so. On this basis, the furthest

shifted feature is again assigned to O_{eq} . None of the other environments are fully attenuated by the longer rf pulse. Thus, the remaining five paramagnetic sites are all assigned to (distorted) O_{ax} sites, for which $C_Q < 4.6$ MHz (Table 1).

The five distinct O_{ax} features resolved by MATPASS experiments are extremely suggestive of the split O_{ax} sites obtained from DFT. Here, we do not necessarily imply that the experimental axial environments correspond to the geometries depicted in Figure 2, but rather that the presence of some form of axial displacement is consistent with the splitting of O_{ax} features in the spectra. For completeness we "assign" four of the five experimental O_{ax} features to the $O_{\text{ax},1}$ - $O_{\text{ax},4}$ sites. The range of experimental and calculated hyperfine shifts is in reasonable agreement, though results from DFT underestimate the experimental values. The otherwise unassigned, highly shifted O_{ax} feature at 5590 ppm (labelled $O_{\text{ax},0}$ in Table 1) could correspond to a structural motif not considered in the DFT calculations, such as an axial oxygen with two nearby interstitials, which would experience a substantial displacement and much larger hyperfine shift. This assertion seems plausible given the higher experimental concentration of interstitials ($\delta = 0.15$ - 0.17) compared to the DFT-optimized supercell ($\delta = 0.125$). It is interesting that the O_{ax} features cluster in well-defined peaks rather than display a broad continuum, suggesting a discrete set of Ni- O_{ax} bond lengths, which may imply a degree of two-dimensional ordering of the interstitial defects. We can compare these results to the neutron diffraction study of Demourgues *et al.* of " $\text{La}_8\text{Ni}_4\text{O}_{17}$ " ($\delta = 0.25$), wherein eight O_{ax} sites are identified, with five distinct Ni- O_{ax} distances.⁸⁵

Relative intensities of split O_{ax} sites in the MATPASS spectra cannot be considered quantitative, as the apparent intensities are inversely weighted by dipolar broadening. That is, sites with large anisotropy have significant intensity distributed across the spinning sideband manifold and so appear smaller in the isotropic slice. The presence of residual spinning sidebands in the isotropic slice, as well as T_2 relaxation effects and the use of a very short recycle delay (50 ms) further complicate quantification. However, the presence of several split features in the spectra implies that most axial oxygens reside in slightly displaced environments.

As a conclusive check, the isotropic shifts obtained from MATPASS were used to model spinning sideband patterns that approximately reproduce the Hahn echo spectra recorded at 40 kHz, with both short ($\pi/6$) and long ($\pi/2$) rf pulse lengths (upper traces, Figure 3) as described in more detail in the SI (Figure S6).

3.5. Variable-temperature NMR ($\leq 150^\circ\text{C}$). We hypothesize that the orthorhombic-to-tetragonal phase transition near 150°C may be associated with changes in the local distortion of the O_{ax} environments induced by motion of nearby O_i . To test this conjecture, we employ ^{17}O VT-NMR as a probe of thermally-activated oxygen motion in $\text{La}_2\text{NiO}_{4+\delta}$. As technical restrictions limit the concurrent use of fast MAS and sample heating, the following spectra have been acquired under slower spinning (12.5 kHz).

Focus on interstitial site. We first study the variable-temperature behavior of the interstitial oxide site at ~ 535 ppm, choosing a field strength of 16.4 T. (This feature moves by $\sim +3$ ppm at high field.) At such a large field, though the paramagnetic features (O_{ax} , O_{eq}) broaden and become difficult to separate, more spinning sidebands arise for the O_i feature, potentially providing detailed information about the local geometry of this site.

Figure 4 shows the ^{17}O MAS NMR spectra of the interstitial oxide site in $\text{La}_2\text{NiO}_{4+\delta}$ from room temperature to 134°C . The most salient change in the spectra is a slight broadening and a loss of signal at and above 80°C , especially between 94°C and 107°C (Figure 4a). At the highest temperature measured (134°C), at most, 3% of the initial intensity remains. Concurrent with the loss of O_i signal at 107°C and 134°C , a broad, asymmetric shoulder appears at a higher frequency of approximately 30 ppm, at 565 ppm (Figure 4b). The resonance falls between the pseudo-tetrahedral interstitial environment of $\text{La}_2\text{NiO}_{4+\delta}$ at 535 ppm and the tetrahedrally-coordinated oxygen environment of La_2O_3 previously reported at 584 ppm.⁷¹ Among OLa_4 sites with known ^{17}O shifts (only $\text{La}_2\text{NiO}_{4+\delta}$ in this work, $\text{LaO}(\text{OH})$, and La_2O_3), the shift moves to higher frequency with reduction of the average O-La bond length and an increase in local tetrahedral symmetry.⁸⁶ A shift of 565 ppm is therefore suggestive of OLa_4 in a less stretched and distorted environment as compared to O_i in $\text{La}_2\text{NiO}_{4+\delta}$, although not as symmetric as in La_2O_3 . On this basis, we tentatively suggest that the feature at 565 ppm arises from OLa_4 sites in a slightly distorted La_2O_3 phase at the surface of the $\text{La}_2\text{NiO}_{4+\delta}$ particles. (This feature is not due to a separate bulk La_2O_3 phase, as the 584 ppm shift of OLa_4 in bulk La_2O_3 remains at this shift with increase in temperature; see Figure S15.) The existence of a La-enriched surface layer is consistent with reports on the unexpectedly strong preference for AO termination in ABO_3 perovskites, and has moreover been observed experimentally in $\text{La}_2\text{NiO}_{4+\delta}$ *via* SIMS-LEIS.^{87,88} Lastly, on cooling to room temperature (red trace, Figure 4a), the O_i signal returns at 535 ppm with, remarkably, nearly quantitative (98%) recovery of the original integrated intensity. We argue in Section 4.1 that the intensity changes are consistent with a motional process involving the interstitial defects.

Broadband spectra. To correlate the onset of interstitial motion with mechanistic details by probing temperature-dependent changes in the paramagnetic sites, we have recorded broadband spectra at similar temperatures. Here, a lower field strength (7.05 T), and thus narrower spectral width, ensures that some signal is recorded from all sites (O_{eq} , O_{ax} , and O_i) when acquiring from a single rf carrier frequency. This central-carrier approach obviates a time-consuming spin-echo mapping experiment, though also preventing quantitative comparison of intensities between different sites.

The broadband VT spectra (Figure 5) display a complex temperature-dependent behavior that, for convenience, we sequentially describe in terms of the diamagnetic region (near O_i), the near paramagnetic region (near O_{ax}), and the far paramagnetic region (near O_{eq}). A significant loss of intensity occurs across all sites with increasing temperature, such that the spectra in Figure 5 are scaled arbitrarily to present similar overall signal strength.

In the diamagnetic region, signal from O_i at 532 ppm decreases with increasing temperature. The absolute integrated intensity of O_i shows a qualitatively similar loss as a function of temperature as seen at high field. As before, the O_i feature vanishes in the high-temperature spectra (130°C and 140°C), revealing the 565 ppm shoulder near O_i . Weak features at 380 ppm (ZrO_2 sample holder⁸⁹) and 170 ppm (LaAlO_3 impurity) are also rendered more obvious at these temperatures in the absence of overlap by spinning sidebands of O_i (see Figure S9).

The near paramagnetic region at modest temperatures (to 110°C) shows a moderate loss of signal at O_{ax} , which is slightly more pronounced than that for O_i , concurrent with the appearance of

spinning sidebands on top of the broad underlying paramagnetic feature. The positions of these spinning sidebands are highly temperature-dependent, and they are not associated with the fixed-position O_i feature. Above 110°C, a major narrowing of the O_{ax} site occurs, centering the shift at 3650 ppm, and revealing a minor feature at 2400 ppm. Moreover, small spinning sidebands associated with this latter feature appear at lower frequencies (between 2200 ppm and 800 ppm).

Finally, the far paramagnetic region is characterized by a decrease in intensity but very little change in the lineshape until above 110°C, where the O_{eq} site suddenly sharpens and grows in intensity relative to O_{ax} . This narrowing is so profound that, at 140°C, spinning sidebands flank either side of the isotropic shift, and the apparent isotropic shift also moves to lower frequency (6000 ppm). Higher-frequency features are observed out to 8000 ppm and are approximately spaced at the MAS rate relative to the O_{eq} isotropic shift indicating that they correspond to the satellite transitions of O_{eq} .

4. Discussion

4.1. Kinetics of interstitial motion. One can postulate several reasons for the dramatic loss of the interstitial feature on heating (Figure 4), such as changes in the Boltzmann distribution of spin states or the physical removal (outgassing) of ^{17}O as O_2 . The first case proves unlikely, as a decrease in the population difference of the central transition spin states on heating from 35 to 134°C (308 to 407 K) can only diminish the signal by at most about 25% (as the spin population difference varies essentially linearly with temperature). Notably, the previously assigned $LaAlO_3$ impurity feature at 170 ppm retains the majority of its intensity with increase in temperature (Figure S8), which is consistent with this. We also discount the gaseous elimination of ^{17}O at elevated temperature, because the recovery of the original spectrum on cooling suggests that the post-VT sample remains comparably ^{17}O -enriched.

Instead, we propose that the spectral changes in Figure 4 are consistent with the onset of oxide-ion dynamics on the NMR timescale, namely, exchange between the interstitial site and a paramagnetic oxygen environment. In an ideal, thermally-activated two-site exchange, as the exchange rate increases, the two spectral features broaden and eventually coalesce. Furthermore, rapid exchange enhances spin dephasing and leads to greatly reduced T_2 relaxation times. This in turn induces significant loss of spectral intensity in multiple-pulse NMR sequences such as the Hahn echo experiments performed here.

Assuming thermally-activated (Arrhenius-type) exchange, in the so-called slow motion or "visit-limited" regime of the Meiboom chemical exchange model,^{90,91}

$$\log I = \log I_0 - \frac{2\tau}{c} A_0 [\exp(-1/T)]^{E_a/R}, \quad (\text{Eq. 3})$$

where I is the integrated signal intensity as observed experimentally, T is the sample temperature, E_a is the activation energy, and the other variables are experimental constants or proportionality constants: I_0 is the integrated signal intensity from a one-pulse experiment, τ is the (fixed) rotor period, $c = k_{ex} \cdot T_2$ (where k_{ex} is the exchange rate), A_0 is the Arrhenius pre-exponential factor, and R is the gas constant. (For derivation and further details see SI, section 3.) Analyzing the loss of integrated O_i intensity in this way (after first subtracting the intensity belonging to the surface OLa_4 sites at 565 ppm), we extract an E_a for interstitial motion equal to 0.59 ± 0.07 eV

(see SI, section 3 and Figure S11). This result agrees well with the MD-simulated value of 0.51 eV given by Chronopoulos *et al.* for exchange between axial and interstitial sites,⁴⁵ as well as a value of 0.54 eV for oxygen self-diffusion in polycrystalline $La_2NiO_{4+\delta}$ as determined by TOF-SIMS.⁹² We thus assign this motional process to interstitial-axial exchange. We note, however, that our activation energy is calculated over a much lower temperature range (<134°C) than in the previous literature (350–700°C).

Asymmetric two-site exchange simulations⁹³ (Figure S12) were performed to explore the effect of exchange between the interstitial and axial anions on the observed lineshapes. We estimate a conservative upper bound $k_{ex} < 320$ kHz for this process, with the correlation time for interstitial jumps no shorter than 3.2 μ s, at 134°C.

4.2. Analysis of broadband variable-temperature spectra. The complex lineshape changes in the paramagnetic features (Figure 5) allow us to explore the onset of oxygen motion in the context of the reported orthorhombic-tetragonal phase transition near 150°C. The most prominent change in the spectra is the sudden narrowing of the O_{eq} feature at 130°C, which suggests a much smaller distribution of isotropic, time-averaged hyperfine shifts. The further increase in the O_{eq} centerband intensity at 140°C also indicates a significant lessening of sources of spectral anisotropy such as electron-nuclear dipolar broadening. We assign the O_{eq} lineshape changes to the rocking motion of NiO_6 octahedra entering the fast motion regime at, or nearly at, the phase transition temperature. On the basis of the maximum frequency separation between O_{eq} sites of ~2000 ppm \approx 82 kHz seen at room temperature, we calculate that the motional rate of rocking exceeds 180 kHz ($= \pi / \sqrt{2} \cdot 82$ kHz)⁹⁴ at 130°C.

The previous neutron diffraction study by Skinner has also resolved a significant loss of anisotropy of the equatorial oxygen site near the phase transition temperature.⁴¹ In that work, the O_{eq} thermal factors at 25°C show a significant c -axis displacement ($U_{33}/U_{11} \approx 2$, $U_{33}/U_{22} \approx 5$), similar to the out-of-plane equatorial distortion depicted in Figure 2. At and above 150°C, however, the O_{eq} thermal ellipsoid appears isotropic. Here, the VT-NMR spectra corroborate the collapse of the O_{eq} environment to an isotropic (in-plane) environment at these temperatures, consistent with fast rocking of the NiO_6 octahedra.

The O_{ax} site similarly narrows at and above 130°C (Figure 5) to a feature approximately at the average of the distorted O_{ax} environments resolved by MATPASS experiments (shown in Figure 3), which suggests a lessening (or time-averaging) of the mean O_{ax} distortion. We attribute this change to a similar motional mechanism, *i.e.* local rocking of NiO_6 octahedra, while noting that simultaneous exchange with interstitial sites competes by contributing to broadening of this site (relative to O_{eq} , which does not exchange at these temperatures). Furthermore, the O_{ax} dynamics are likely subject to a distribution of motional correlation times. The presence of spinning sidebands at lower temperatures (~70°C), for example, suggests a partial averaging of a subset of the distorted O_{ax} environments by motion already in the fast exchange limit. In previous VT-NMR studies of anionic conductors, the coexistence of multiple correlation times has been attributed to vacancy-dopant ordering or to the presence of mobile and rigid domains with differing defect concentrations.^{18,95} In this system, the apparent variation in O_{ax} motional rates likely results from the larger population of axial sites relative to that of the interstitial defects with which they exchange.⁹⁶

The influence of interstitial motion on the dynamics of the O_{ax} and O_{eq} sites can be inferred in several ways. We note that the calculated motional rate of NiO_6 rocking (in excess of 180 kHz) is near the coalescence regime for interstitial–axial exchange (Figure S12), suggesting that near the phase transition temperature, the exchange motion is coupled to the octahedral rocking (or vice versa). Secondly, clearly shown in the DFT calculations and, experimentally from the distribution of shifts, the O_{ax} distortion arises from proximity to interstitial defects, and therefore the long-range motion of interstitials necessarily contributes to averaging of the O_{ax} distortion. We conclude that the loss, or significant reduction of, the local O_i -induced distortion occurs at or near the phase transition and is moreover correlated with exchange between interstitial and axial sites.

4.3. Extension to other systems and higher temperatures.

The VT-NMR results clarify that the previously observed orthorhombic–tetragonal phase transition arises from the loss of a local structural distortion that is correlated with rapid oxide-ion dynamics. It remains unclear how this distortion leads to the cooperative tilting of perovskite layers in the bulk and thus the low-temperature orthorhombic structure, but we note that even for very subtle phase transitions, VT-NMR spectra should resolve the relevant motional changes that drive the transition. An example system is the related phase $La_2NiO_{4.11-4.13}$, which undergoes a subtle transition at ~ 300 K with both low- and high-temperature phases nominally tetragonal, but with long-range 3D interstitial ordering only apparent below 300 K.⁹⁷ The sensitivity of the NMR spectra could in this case provide a convenient check on the interplay of oxygen motion and interstitial ordering, even where the latter property is not readily apparent by diffraction or other techniques.

Work is in progress to acquire and assign high-temperature (150°C – 800°C) ^{17}O NMR spectra of $La_2NiO_{4+\delta}$ to explore motion involving exchange between all of the oxygen sites and to examine the effect of temperature on oxygen interstitial content.

5. Conclusion

A combined experimental (NMR spectroscopy) and computational (DFT) methodology has been employed to clarify the local structure and dynamics of the mixed ionic–electronic conductor $La_2NiO_{4+\delta}$ to obtain ^{17}O MAS NMR spectra of a paramagnetic oxide in the solid state. Our main conclusions are as follows:

- (1) Small compositional changes in $La_2NiO_{4+\delta}$ occur as a result of ^{17}O -enrichment; we observe an increase in the oxygen excess (before: $\delta = 0.12$ – 0.14 ; after: $\delta = 0.15$ – 0.17 by XRD, $\delta = \sim 0.2$ by quantitative NMR) and the formation of small amounts (~ 3 wt. %) of an impurity assigned to the higher-order $La_4Ni_3O_{10}$ phase.
- (2) Room-temperature ^{17}O MAS NMR spectra of ^{17}O -enriched $La_2NiO_{4+\delta}$ acquired by spin-echo mapping reveal three distinct oxygen environments assigned to interstitial (O_i), axial (O_{ax}) and equatorial (O_{eq}) sites, with quantitative measurements suggesting fully stochastic ^{17}O -enrichment.

- (3) DFT calculations of $La_2NiO_{4+\delta}$ provide local structural insight and are used to obtain Fermi contact (hyperfine) shifts and quadrupolar coupling constants that corroborate the assignment of the experimental spectra. In particular, paramagnetic O_{eq} and O_{ax} features can be distinguished on the basis of the much larger C_Q of the former (4.7 MHz vs. ~ 1.1 MHz).
- (4) High-resolution MATPASS NMR spectra, in combination with quadrupolar filtering techniques, reveal the splitting of the O_{ax} site into five discrete axial environments (3640–5590 ppm). Our DFT calculations also show a similar clustering of four distinct O_{ax} shifts, which can be rationalized on the basis of Ni– O_{ax} distances. We demonstrate that this axial splitting arises from a local structural distortion directly induced by the interstitial defect.
- (5) Variable-temperature NMR spectra at high field resolve the (reversible) loss of the interstitial oxide feature due to a thermally-activated motional process with $E_a = 0.59 \pm 0.07$ eV; we assign this motion to exchange with axial sites.
- (6) Analysis of the entire broadband spectrum as a function of temperature allows us to elucidate the types of motion and exchange affecting the interstitial, axial, and equatorial oxygen sites. In brief, exchange between interstitial and axial sites dominates the intensity loss of the O_i resonance. Local rocking motion of NiO_6 octahedra, with associated averaging effects on axial and equatorial displacement, is dominant for the O_{ax} and O_{eq} lineshapes, with a motional rate larger than 180 kHz at 130°C . Abrupt changes in the VT-NMR spectra are associated with approach to the previously reported orthorhombic-to-tetragonal phase transition of $La_2NiO_{4+\delta}$, these changes occurring here between 110°C and 130°C . We observe a significant reduction in the magnitude of local structural distortions due to NiO_6 octahedral motion, correlated with interstitial–axial exchange, at the phase transition temperature; this illustrates how oxide-ion motion at the atomic level directly influences the phase transition in the bulk.

The design of next-generation MIECs with improved oxide-ion conductivity relies on a fundamental understanding of the underlying anion dynamics across a wide temperature range, which ^{17}O VT-NMR spectroscopy is uniquely poised to resolve. Work is ongoing to obtain high-temperature spectra ($> 150^\circ\text{C}$) of $La_2NiO_{4+\delta}$ to obtain insight into oxygen conduction mechanisms in the conditions most relevant for IT-SOFC and sensor operation. We also anticipate that cation doping of perovskite MIECs, a common strategy in tuning material properties such as the electronic and ionic conductivity, will have significant effects on the paramagnetic ^{17}O spectra and allow for comprehensive depictions of the local structure and dynamics, as well as the fundamental defect chemistry, of these functionally relevant oxides.

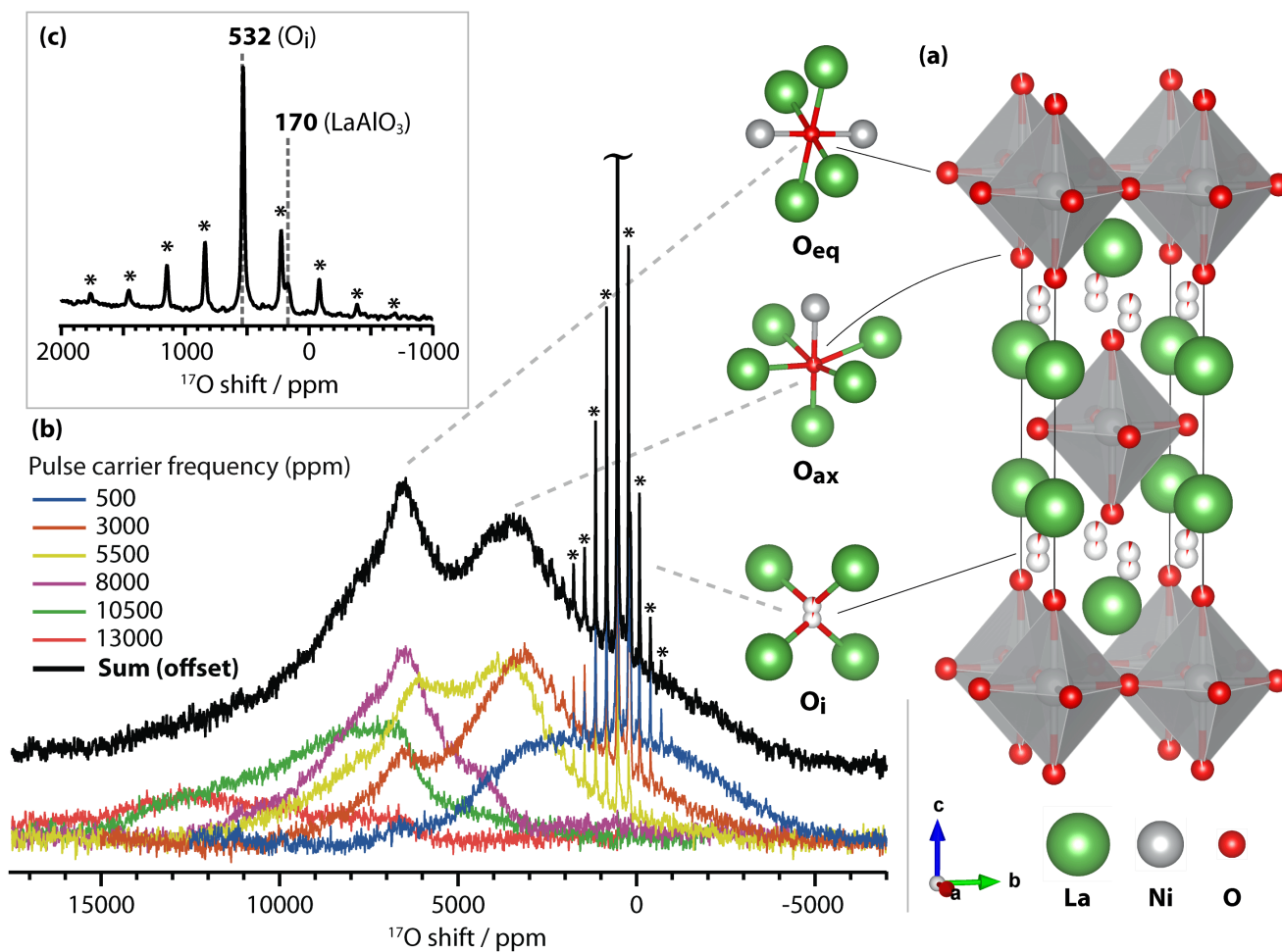


Figure 1. Room temperature ^{17}O MAS-NMR spectrum of $\text{La}_2\text{NiO}_{4+\delta}$ with proposed assignments. (a) Crystal structure of the high-temperature tetragonal (space group $I4/mmm$) phase of $\text{La}_2\text{NiO}_{4.17}$ as reported by Skinner *et al.*⁴¹ Partially occupied sites (O_{ax} , O_{i}) are depicted as partially filled spheres. (b) Individual sub-spectra collected at different offset frequencies (colored) summed to give the broadband spin-echo mapping spectrum (black). Proposed assignments depict the local geometry about each oxygen environment (equatorial O_{eq} , axial O_{ax} , and interstitial O_{i}). A rotor-synchronized Hahn echo pulse sequence ($\pi/6 - \tau - \pi/3 - \tau$ -acquire) was used for each sub-spectrum. Spectra were collected at 7.05 T at a MAS rate of 12.5 kHz, with 120,000 scans per sub-spectrum and a recycle delay of 0.5 s. Asterisks denote spinning sidebands. (c) Inset showing the "diamagnetic region" of the summed spin-echo mapping spectrum in (b). Features at 532 ppm and 170 ppm are assigned to interstitial oxygen (O_{i}) in $\text{La}_2\text{NiO}_{4+\delta}$, and a LaAlO_3 impurity phase, respectively. Asterisks denote spinning sidebands.

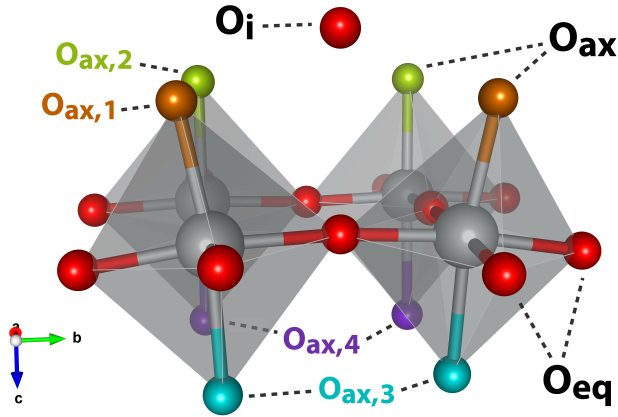


Figure 2. Local structural distortion induced by nearby interstitial defect (O_i), from part of the DFT-optimized $La_{16}Ni_8O_{33}$ supercell. Axial sites (in orange) closest to the interstitial undergo the largest displacement towards the Ni center, with concomitant tilting of the NiO_6 octahedra. The four types of axial oxygen sites, ordered by increasing Ni– O_{ax} bond length, are depicted in orange ($O_{ax,1}$), green ($O_{ax,2}$), cyan ($O_{ax,3}$) and purple ($O_{ax,4}$). Nickel atoms are depicted in grey and non-axial (equatorial) oxygen atoms in red. (For clarity only part of the structure is shown, omitting La.)

Table 1. Calculated and experimental structural and ^{17}O NMR parameters (computed Ni–O bond lengths, experimental isotropic chemical shifts $\delta_{iso,exp}$, calculated Fermi contact shifts $\delta_{FC,calc}$, and quadrupolar coupling constants C_Q) for $La_2NiO_{4+\delta}$ at room temperature.

	Ni–O dist. (Å)	$\delta_{iso,exp}$ (ppm)	$\delta_{FC,calc}$ (ppm)	C_Q (MHz)	
				Exp	Calc
O_{eq}	~1.9 (avg)	~6500; 6860(6) (MATPASS)	10322	≥ 4.6	4.73
O_{ax}	~2.2 (avg)	~3500	3539 (avg)	< 4.6	1.14 (avg)
$O_{ax,0}$	—*	5590(5)	—*	< 4.6	—*
$O_{ax,1}$	2.13	4775(4)	3914	< 4.6	2.35
$O_{ax,2}$	2.16	4315(3)	3821	< 4.6	1.09
$O_{ax,3}$	2.24	3960(3)	3234	< 4.6	0.67
$O_{ax,4}$	2.26	3640(2)	3189	< 4.6	0.46
O_i	— [†]	532(1)	19	< 4.6	0.38

Standard errors in the fitted experimental shifts are given in parentheses. *Not observed in DFT-optimized supercell. [†]Not bonded to Ni.

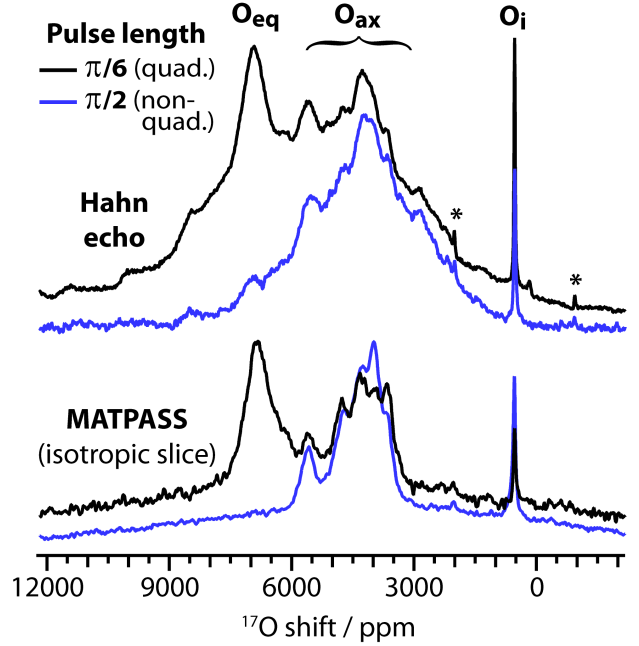


Figure 3. Comparison of Hahn echo and MATPASS NMR spectra of $La_2NiO_{4+\delta}$, with quadrupolar filtering. Spectra were acquired at 4.7 T with a MAS rate of 40 kHz. Splitting of O_{ax} is partially resolved in the Hahn echo and fully resolved in the MATPASS data. Both experiments show pulse length dependence ($\pi/6$ vs. $\pi/2$) consistent with a single highly quadrupolar environment (O_{eq}). Asterisks denote spinning sidebands where apparent.

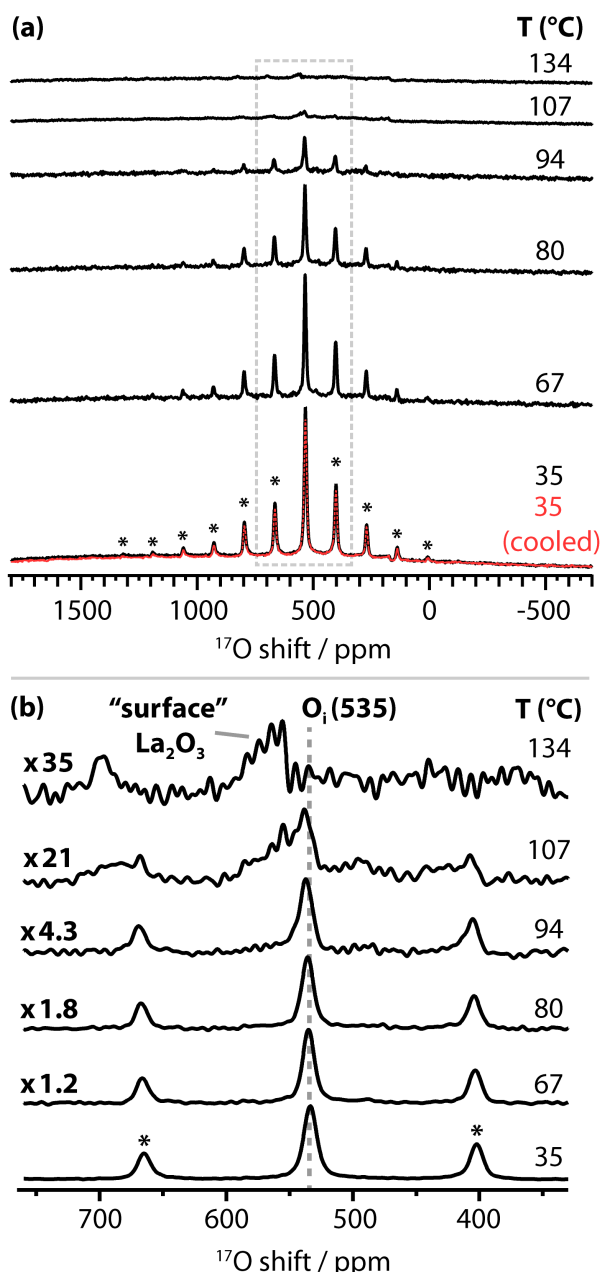


Figure 4. Variable-temperature NMR spectra of $\text{La}_2\text{NiO}_{4+\delta}$, focusing on the interstitial oxygen site. (a, top to bottom) ^{17}O MAS-NMR spectra of $\text{La}_2\text{NiO}_{4+\delta}$ acquired at the indicated temperatures, and at 35 °C after cooling from high temperature (red). The difference between normal room temperature and the lowest sample temperature (35°C) is due to frictional heating by MAS. Spectra were acquired at 16.4 T under a MAS rate of 12.5 kHz. Spectra shown are normalized to the number of scans. (b) Detail of (a) with spectra scaled to highlight broadening and shift of interstitial site. Asterisks denote spinning sidebands (for clarity shown only at 35 °C).

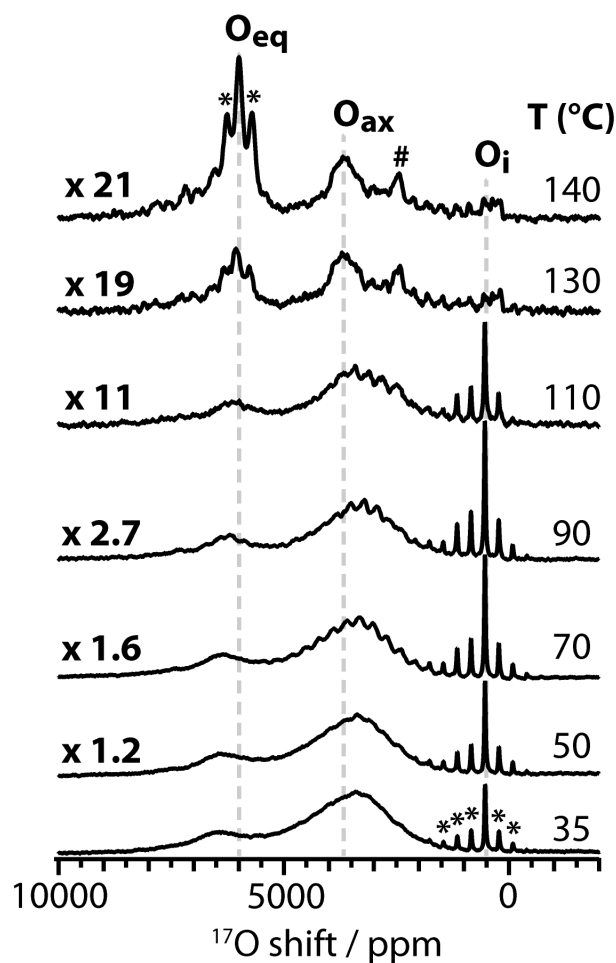


Figure 5. Broadband variable-temperature NMR spectra of $\text{La}_2\text{NiO}_{4+\delta}$. Spectra were acquired at 7.05 T at a MAS rate of 12.5 kHz. Spectra were normalized to number of scans (between ~300,000 and ~6,700,000 per spectrum) and then scaled as shown to obtain similar intensity for the O_{ax} feature (~3500 ppm) present in all spectra. # indicates the feature at 2400 ppm assigned to the $\text{La}_3\text{Ni}_2\text{O}_7/\text{La}_4\text{Ni}_3\text{O}_{10}$ impurity phase (see SI, section 5). Asterisks denote visible spinning sidebands, for clarity only indicated for O_i at 35 °C and for O_{eq} at 140 °C. (A close-up view of the spectrum at 140°C depicting the weakly resolved peaks in the diamagnetic region is shown in Figure S9.)

ASSOCIATED CONTENT

Supporting Information. The Supporting Information is available free of charge on the ACS Publications Website at DOI: [DOI]

Additional details of computational methods, and of the procedure for determining the activation energy (E_a) of interstitial motion; further description of the origin of the local axial distortion; calculation of phase fractions of surface La_2O_3 and the $\text{La}_3\text{Ni}_2\text{O}_7/\text{La}_4\text{Ni}_3\text{O}_{10}$ impurity; powder XRD patterns of $\text{La}_2\text{NiO}_{4+\delta}$ samples and of mixed samples of $\text{La}_2\text{NiO}_{4+\delta}$, NiO , $\text{La}_3\text{Ni}_2\text{O}_7$ and $\text{La}_4\text{Ni}_3\text{O}_{10}$; TGA data under reducing conditions (5% H_2 in N_2), and correlation of the TGA-determined oxygen excess (δ) with refined lattice parameters; depictions of DFT-optimized supercells; quantitative fitting and deconvolution of Hahn echo and MATPASS NMR spectra; the ^{17}O NMR spectrum of a mixed sample of $\text{La}_2\text{NiO}_{4+\delta}$, $\text{La}_3\text{Ni}_2\text{O}_7$ and $\text{La}_4\text{Ni}_3\text{O}_{10}$; comparison of LaAlO_3 impurity intensity across various samples and with temperature; close-up view of the diamagnetic region of the high-

temperature broadband NMR spectra of $\text{La}_2\text{NiO}_{4+\delta}$; temperature dependence of the ^{17}O NMR shifts of La_2O_3 ; Arrhenius-like plots for the calculation of E_a for interstitial motion; and asymmetric two-site simulations of exchange between axial and interstitial oxygen environments.

AUTHOR INFORMATION

Corresponding Author

*E-mail: cpg27@cam.ac.uk.

Notes

The authors declare no competing financial interest.

ACKNOWLEDGMENTS

Via membership of the U.K.'s HPC Materials Chemistry Consortium, some computations have made use of ARCHER, the U.K.'s national high-performance computing service, which is funded by the Office of Science and Technology through EPSRC's High End Computing Programme (EPSRC Grant No. EP/L000202). This research also used resources of the Center for Functional Nanomaterials, which is a U.S. DOE Office of Science Facility, at Brookhaven National Laboratory under Contract No. DE-SC0012704. D.M.H. acknowledges funding from the Cambridge Commonwealth Trusts. G.K. thanks the European Research Council for an Advanced Fellowship. F.B. thanks the EU Marie Curie actions for an International Incoming Fellowship 2011–2013 (Grant 275212) and Clare Hall, University of Cambridge, for a Research Fellowship. Sylvia Britto, Evan Keyzer, Alexander C. Forse, Beth Howe, Oliver Pecher, Raphaële J. Clément, George Lane, Ieuan Seymour, Luke Sperrin, and Michael W. Gaultois are acknowledged for useful discussions and support. Additional thanks are due to Michal Leskes (Weizmann Institute of Science) and Andrew J. Pell (Stockholm University) for assistance regarding NMR pulse sequences.

REFERENCES

- (1) Skinner, S. J. *Int. J. Inorg. Mater.* **2001**, *3*, 113–121.
- (2) Tarancón, A.; Burriel, M.; Santiso, J.; Skinner, S. J.; Kilner, J. A. *J. Mater. Chem.* **2010**, *20*, 3799.
- (3) Haugsrud, R.; Norby, T. *Nat. Mater.* **2006**, *5*, 193–196.
- (4) Yang, L.; Wang, S.; Blinn, K.; Liu, M.; Liu, Z.; Cheng, Z.; Liu, M. *Science* **2009**, *326*, 126–129.
- (5) Sengodan, S.; Choi, S.; Jun, A.; Shin, T. H.; Ju, Y.-W.; Jeong, H. Y.; Shin, J.; Irvine, J. T. S.; Kim, G. *Nat. Mater.* **2015**, *14*, 205–209.
- (6) Sunarso, J.; Baumann, S.; Serra, J. M.; Meulenberg, W. A.; Liu, S.; Lin, Y. S.; Diniz da Costa, J. C. *J. Membr. Sci.* **2008**, *320*, 13–41.
- (7) Luo, H.; Efimov, K.; Jiang, H.; Feldhoff, A.; Wang, H.; Caro, J. *Angew. Chem. Int. Edit.* **2011**, *50*, 759–763.
- (8) Huang, K.; Wan, J.; Goodenough, J. B. *J. Mater. Sci.* **2001**, *36*, 1093–1098.
- (9) Shao, Z.; Haile, S. M. *Nature* **2004**, *431*, 170–173.
- (10) Tuller, H. L. *Solid State Ionics* **1997**, *94*, 63–74.
- (11) Chroneos, A.; Yildiz, B.; Tarancón, A.; Parfitt, D.; Kilner, J. A. *Energ. Environ. Sci.* **2011**, *4*, 2774–2789.
- (12) Linford, R. G.; Hackwood, S. *Chem. Rev.* **1981**, *81*, 327–364.
- (13) Reichert, D. *Annu. Rep. NMR Spectrosc.* **2005**, *55*, 159–203.
- (14) Blanc, F.; Spencer, L.; Goward, G. R. *Encyclopedia of Magnetic Resonance: Quadrupolar NMR of Ionic Conductors, Batteries, and Other Energy-related Materials*; Harris, R. K., Ed.; John Wiley & Sons, Ltd: Chichester, UK, 2007.
- (15) O'Dell, L. A.; Ratcliffe, C. I. *Encyclopedia of Magnetic Resonance: Quadrupolar NMR to Investigate Dynamics in Solid Materials*; Harris, R. K., Ed.; John Wiley & Sons, Ltd: Chichester, UK, 2007.
- (16) Kim, N.; Grey, C. P. *Science* **2002**, *297*, 1317–1320.
- (17) Kim, N.; Grey, C. P. *Dalton Trans.* **2004**, 3048–3052.
- (18) Kim, N.; Vannier, R.-N.; Grey, C. P. *Chem. Mater.* **2005**, *17*, 1952–1958.
- (19) Holmes, L.; Peng, L.; Heinmaa, I.; O'Dell, L. A.; Smith, M. E.; Vannier, R.-N.; Grey, C. P. *Chem. Mater.* **2008**, *20*, 3638–3648.
- (20) Blanc, F.; Middlemiss, D. S.; Buannic, L.; Palumbo, J. L.; Farnan, I.; Grey, C. P. *Solid State Nucl. Magn. Reson.* **2012**, *42*, 87–97.
- (21) Kim, G.; Griffin, J. M.; Blanc, F.; Haile, S. M.; Grey, C. P. *J. Am. Chem. Soc.* **2015**, *137*, 3867–3876.
- (22) Fuda, K.; Kishio, K.; Yamauchi, S.; Fueki, K.; Onoda, Y. *J. Phys. Chem. Solids* **1984**, *45*, 1253–1257.
- (23) Spearing, D. R.; Farnan, I.; Stebbins, J. F. *Phys. Chem. Miner.* **1992**, *19*, 307–321.
- (24) Adler, S.; Russek, S.; Reimer, J.; Fendorf, M.; Stacy, A.; Huang, Q.; Santoro, A.; Lynn, J.; Baltisberger, J.; Werner, U. *Solid State Ionics* **1994**, *68*, 193–211.
- (25) Witschas, M.; Eckert, H.; Freiheit, H.; Putnis, A.; Korus, G.; Janßen, M. *J. Phys. Chem. A* **2001**, *105*, 6808–6816.
- (26) Hampson, M. R.; Evans, J. S. O.; Hodgkinson, P. J. *Am. Chem. Soc.* **2005**, *127*, 15175–15181.
- (27) Kim, N.; Hsieh, C.-H.; Huang, H.; Prinz, F. B.; Stebbins, J. F. *Solid State Ionics* **2007**, *178*, 1499–1506.
- (28) Buzlukov, A.; Trokiner, A.; Kozhevnikov, V.; Verkhovskii, S.; Yakubovskiy, A.; Leonidov, I.; Gerashenko, A.; Stepanov, A.; Baklanova, I.; Tankeyev, A. *J. Solid State Chem.* **2011**, *184*, 36–43.
- (29) Kiyono, H.; Matsuda, Y.; Shimada, T.; Ando, M.; Oikawa, I.; Maekawa, H.; Nakayama, S.; Ohki, S.; Tansho, M.; Shimizu, T.; Florian, P.; Massiot, D. *Solid State Ionics* **2012**, *228*, 64–69.
- (30) Chien, P.-H.; Jee, Y.; Huang, C.; Dervişoğlu, R.; Hung, I.; Gan, Z.; Huang, K.; Hu, Y.-Y. *Chem. Sci.* **2016**, *7*, 3667–3675.
- (31) Dervişoğlu, R.; Middlemiss, D. S.; Blanc, F.; Lee, Y.-L.; Morgan, D.; Grey, C. P. *Chem. Mater.* **2015**, *27*, 3861–3873.
- (32) Seymour, I. D.; Middlemiss, D. S.; Halat, D. M.; Trease, N. M.; Pell, A. J.; Grey, C. P. *J. Am. Chem. Soc.* **2016**, *138*, 9405–9408.
- (33) Blanc, F.; Middlemiss, D. S.; Gan, Z.; Grey, C. P. *J. Am. Chem. Soc.* **2011**, *133*, 17662–17672.
- (34) Martel, L.; Magnani, N.; Vigier, J.-F.; Boshoven, J.; Selfslag, C.; Farnan, I.; Griveau, J.-C.; Somers, J.; Fanghänel, T. *Inorg. Chem.* **2014**, *53*, 6928–6933.
- (35) Looyestijn, W. J.; Klaassen, T. O.; Poulis, N. J. *Physica B+C* **1978**, *93*, 349–357.
- (36) Jurkutat, M.; Rybicki, D.; Sushkov, O. P.; Williams, G. V. M.; Erb, A.; Haase, J. *Phys. Rev. B* **2014**, *90*, 140504.
- (37) Bert, F.; Olariu, A.; Zorko, A.; Mendels, P.; Trombe, J. C.; Duc, F.; Vries, M. A. de; Harrison, A.; Hillier, A. D.; Lord, J.; Amato, A.; Baines, C. J. *Phys. Conf. Ser.* **2009**, *145*, 12004.
- (38) Kong, X.; Terskikh, V. V.; Khade, R. L.; Yang, L.; Rorick, A.; Zhang, Y.; He, P.; Huang, Y.; Wu, G. *Angew. Chem. Int. Edit.* **2015**, *54*, 4753–4757.
- (39) Woolley, R. J.; Skinner, S. J. *J. Power Sources* **2013**, *243*, 790–795.
- (40) Demourgues, A.; Wattiaux, A.; Grenier, J. C.; Pouchard, M.; Soubeyroux, J. L.; Dance, J. M.; Hagenmuller, P. *J. Solid State Chem.* **1993**, *105*, 458–468.
- (41) Skinner, S. J. *Solid State Sci.* **2003**, *5*, 419–426.
- (42) Tavares, C. P. *Mater. Res. Bull.* **1985**, *20*, 979–987.
- (43) Ganguly, P.; Rao, C. N. R. *J. Solid State Chem.* **1984**, *53*, 193–216.
- (44) Aguadero, A.; Alonso, J. A.; Martínez-Lope, M. J.; Fernández-Díaz, M. T.; Escudero, M. J.; Daza, L. *J. Mater. Chem.* **2006**, *16*, 3402–3408.
- (45) Chroneos, A.; Parfitt, D.; Kilner, J. A.; Grimes, R. W. *J. Mater. Chem.* **2010**, *20*, 266–270.
- (46) Sayer, M.; Odier, P. *J. Solid State Chem.* **1987**, *67*, 26–36.
- (47) Tamura, H.; Hayashi, A.; Ueda, Y. *Physica C* **1993**, *216*, 83–88.
- (48) Zhang, H. L.; Wu, X. S.; Chen, C. S.; Liu, W. *Phys. Rev. B* **2005**, *71*, 64422.
- (49) Liu, T.; Xu, Y.; Li, Y.; Wang, Z.; Zhao, J. *Ceram. Int.* **2011**, *37*, 3361–3364.

- (50) Larson, A.C.; Von Dreele, R.B. *General Structure Analysis System (GSAS)*; Los Alamos National Laboratory Report LAUR 86-748; Los Alamos National Laboratory: Los Alamos, NM, 2000.
- (51) Toby, B. H. *J. Appl. Crystallogr.* **2001**, *34*, 210–213.
- (52) Boehm, E.; Bassat, J.-M.; Steil, M. C.; Dordor, P.; Mauvy, F.; Grenier, J.-C. *Solid State Sci.* **2003**, *5*, 973–981.
- (53) Hung, I.; Zhou, L.; Pourpoint, F.; Grey, C. P.; Gan, Z. *J. Am. Chem. Soc.* **2012**, *134*, 1898–1901.
- (54) Bielecki, A.; Burum, D. P. *J. Magn. Reson. Ser. A* **1995**, *116*, 215–220.
- (55) Beckmann, P. A.; Dybowski, C. *J. Magn. Reson.* **2000**, *146*, 379–380.
- (56) *Topspin 3.2, software for NMR spectral analysis*; Bruker Biospin: Rheinstetten, Germany, 2012.
- (57) Massiot, D.; Fayon, F.; Capron, M.; King, I.; Le Calvé, S.; Alonso, B.; Durand, J.-O.; Bujoli, B.; Gan, Z.; Hoatson, G. *Magn. Reson. Chem.* **2002**, *40*, 70–76.
- (58) Dovesi, R.; Saunders, V. R.; Roetti, C.; Orlando, R.; Zicovich-Wilson, C. M.; Pascale, F.; Civalleri, B.; Doll, K.; Harrison, N. M.; Bush, I. J. *CRYSTAL09 User's Manual*; University of Torino: Torino, Italy, 2010.
- (59) Winkler, E.; Rivadulla, F.; Zhou, J.-S.; Goodenough, J. B. *Phys. Rev. B* **2002**, *66*, 94418.
- (60) Pyykkö, P. *Mol. Phys.* **2008**, *106*, 1965–1974.
- (61) Kim, J.; Middlemiss, D. S.; Chernova, N. A.; Zhu, B. Y. X.; Masquelier, C.; Grey, C. P. *J. Am. Chem. Soc.* **2010**, *132*, 16825–16840.
- (62) Zhang, Y.; Castets, A.; Carlier, D.; Ménétrier, M.; Boucher, F. *J. Phys. Chem. B* **2012**, *116*, 17393–17402.
- (63) Ganguly, P.; Kollai, S.; Rao, C. N. R. *Magn. Lett.* **1980**, *1*, 107.
- (64) Goodenough, J. B.; Ramasesha, S. *Mater. Res. Bull.* **1982**, *17*, 383–390.
- (65) Aguadero, A.; Pérez, M.; Alonso, J. A.; Daza, L. *J. Power Sources* **2005**, *151*, 52–56.
- (66) Rice, D. E.; Buttrey, D. J. *J. Solid State Chem.* **1993**, *105*, 197–210.
- (67) Tamura, H.; Hayashi, A.; Ueda, Y. *Physica C* **1996**, *258*, 61–71.
- (68) Sayers, R.; Skinner, S. J. *J. Mater. Chem.* **2010**, *21*, 414–419.
- (69) Massiot, D.; Farnan, I.; Gautier, N.; Trumeau, D.; Trokner, A.; Coutures, J. P. *Solid State Nucl. Magn. Reson.* **1995**, *4*, 241–248.
- (70) Pell, A. J.; Clément, R. J.; Grey, C. P.; Emsley, L.; Pintacuda, G. *J. Chem. Phys.* **2013**, *138*, 114201.
- (71) Yang, S.; Shore, J.; Oldfield, E. *J. Magn. Reson.* **1992**, *99*, 408–412.
- (72) Jorgensen, J. D.; Dabrowski, B.; Pei, S.; Richards, D. R.; Hinks, D. G. *Phys. Rev. B* **1989**, *40*, 2187–2199.
- (73) Bastow, T. J.; Dirken, P. J.; Smith, M. E.; Whitfield, H. J. *J. Phys. Chem.* **1996**, *100*, 18539–18545.
- (74) Nordenskiöld, L.; Laaksonen, A.; Kowalewski, J. *J. Am. Chem. Soc.* **1982**, *104*, 379–382.
- (75) Oldfield, E.; Coretsopoulos, C.; Yang, S.; Reven, L.; Lee, H. C.; Shore, J.; Han, O. H.; Ramli, E.; Hinks, D. *Phys. Rev. B* **1989**, *40*, 6832–6849.
- (76) Went, M. S.; Reimer, J. A. *Chem. Mater.* **1990**, *2*, 389–394.
- (77) Kentgens, A. P. M. *Geoderma* **1997**, *80*, 271–306.
- (78) Massiot, D.; Bessada, C.; Coutures, J. P.; Taulelle, F. *J. Magn. Reson.* **1990**, *90*, 231–242.
- (79) Frayret, C.; Villesuzanne, A.; Pouchard, M. *Chem. Mater.* **2005**, *17*, 6538–6544.
- (80) Takeda, Y.; Kanno, R.; Sakano, M.; Yamamoto, O.; Takano, M.; Bando, Y.; Akinaga, H.; Takita, K.; Goodenough, J. B. *Mater. Res. Bull.* **1990**, *25*, 293–306.
- (81) Seo, D.-H.; Lee, J.; Urban, A.; Malik, R.; Kang, S.; Ceder, G. *Nat. Chem.* **2016**, *8*, 692–697.
- (82) Gerotheranassis, I. P. *Prog. Nucl. Magn. Reson. Spectrosc.* **2010**, *57*, 1–110.
- (83) Hu, Y.-Y.; Levin, E. M.; Schmidt-Rohr, K. *J. Am. Chem. Soc.* **2009**, *131*, 8390–8391.
- (84) Kentgens, A. P. M. *Encyclopedia of Magnetic Resonance: Quadrupolar Nutation Spectroscopy*; Harris, R. K., Ed.; John Wiley & Sons, Ltd: Chichester, UK, 2007.
- (85) Demourgues, A.; Weill, F.; Darriet, B.; Wattiaux, A.; Grenier, J. C.; Gravereau, P.; Pouchard, M. *J. Solid State Chem.* **1993**, *106*, 317–329.
- (86) Ali, F.; Smith, M. E.; Steuernagel, S.; Whitfield, H. J. *J. Mater. Chem.* **1996**, *6*, 261–264.
- (87) Druce, J.; Téllez, H.; Burriel, M.; Sharp, M. D.; Fawcett, L. J.; Cook, S. N.; McPhail, D. S.; Ishihara, T.; Brongersma, H. H.; Kilner, J. A. *Energ. Environ. Sci.* **2014**, *7*, 3593–3599.
- (88) Wu, J.; Pramana, S. S.; Skinner, S. J.; Kilner, J. A.; Horsfield, A. P. *J. Mater. Chem. A* **2015**, *3*, 23760–23767.
- (89) Bastow, T. J.; Stuart, S. N. *Chem. Phys.* **1990**, *143*, 459–467.
- (90) Meiboom, S. *J. Chem. Phys.* **1961**, *34*, 375–388.
- (91) Brooks, R. A. *Magn. Reson. Med.* **2002**, *47*, 388–391.
- (92) Sayers, R.; De Souza, R. A.; Kilner, J. A.; Skinner, S. J. *Solid State Ionics* **2010**, *181*, 386–391.
- (93) Bain, A. D. *MEXICO: The McMaster Program for Exchange Line-shape Calculations*; McMaster University, Hamilton, Ont., Canada, 2002.
- (94) Bain, A. D. *Prog. Nucl. Magn. Reson. Spectrosc.* **2003**, *43*, 63–103.
- (95) Wang, F.; Grey, C. P. *J. Am. Chem. Soc.* **1998**, *120*, 970–980.
- (96) Adler, S. B.; Smith, J. W.; Reimer, J. A. *J. Chem. Phys.* **1993**, *98*, 7613–7620.
- (97) Tranquada, J. M.; Kong, Y.; Lorenzo, J. E.; Buttrey, D. J.; Rice, D. E.; Sachan, V. *Phys. Rev. B* **1994**, *50*, 6340.

Insert Table of Contents artwork here

